Model-Free-Predictive Control of Open-End Winding Synchronous Reluctance Motor Drive

1st Filippo Gemma
Electrical, Computer and Biomedical Engineering Dept
University of Pavia
Pavia, IT
filippo.gemma01@universitadipavia.it

2nd Jacopo Riccio
Power electronics, machines and control group
University of Nottingham
Nottingham, UK
Jacopo.Riccio2@nottingham.ac.uk

3rd Andrea Volpini
Electrical, Computer and Biomedical Engineering Dept
University of Pavia
Pavia, IT
andrea.volpini01@universitadipavia.it

4th Giulia Tresca
Electrical, Computer and Biomedical Engineering Dept
University of Pavia
Pavia, IT
giulia.tresca@unipv.it

5th Pericle Zanchetta
Electrical, Computer and Biomedical Engineering Dept
University of Pavia
Pavia, IT
pericle.zanchetta@unipv.it

***Abstract*—This paper presents a Model-Free Predictive Control (MFPC) strategy for Synchronous Reluctance Machines (SyRel) with an Open-End Winding (OEW) configuration. The method enhances performance by ensuring accurate torque and speed tracking in both transient and steady-state conditions. The OEW topology, combined with MFPC, enables extended base speed operation, active regulation of the Floating Capacitor (FC) voltage, and unity power factor, without requiring detailed motor parameters.**

The proposed control relies on a Finite-Control-Set Model-Free Predictive Control (MFPC) strategy with a unified cost function to regulate torque, FC voltage, and Main side power factor. System predictions are obtained via an Auto-Regressive with Exogenous input (ARX) model, whose parameters are estimated online using a Recursive Least Squares (RLS) algorithm, ensuring robustness to parameter variations. Simulation results confirm the effectiveness of the proposed control strategy. A comparative analysis with conventional Model-Based Predictive Control demonstrates the superior performance, improved robustness, and reduced complexity of the MF approach, making it a promising solution for high-performance SyRel OEW drives.

***Index Terms*—Finite-Control-Set, Model-Free-Predictive Control, Open-End Winding, Synchronous Reluctance Machine, Floating Capacitor, Auto-Regressive with Exogenous input, Recursive Least Squares.**

I. Introduction

Synchronous Reluctance motor drives are emerging as a competitive alternative to Induction and Permanent Magnet Synchronous Motor (IM and PMSM) drives in many applications [1]. Their popularity is driven by high dynamic performance, compact size, competitive costs, and the absence of rare-earth permanent magnets [2].

Despite these advantages, SyRel drives face technical challenges such as low power factor, limited constant power speed range, high torque ripple, and strong magnetic non-linearities that complicate control [3], [4].

One effective way to improve the performance of SyRel drives is to adopt an Open-End Winding configuration, where both ends of each winding are connected to two three-phase inverters [5], [6]. This setup allows achieving higher voltage utilization and increased active power at the same rotational speed. This is made possible through the optimal management of active and reactive power across the two machine terminals. The complete system structure is shown in Fig. 1, where the motor windings are powered by a Main Converter (Main-Conv) and an Auxiliary Converter (Aux-Conv).

Different DC-link configurations for the auxiliary converter have been proposed, each with specific advantages and limitations. The first is the shared DC-link configuration between the two inverters [7], [8], which offers a compact hardware solution and inherent fault tolerance. However, this topology limits the achievable operating range, as the voltage available at the machine terminals is constrained by the common DC-link, and it is also prone to circulating zero-sequence currents. These currents can be mitigated with complex modulation strategies, though this often reduces the voltage transfer ratio. If left unaddressed, the system may experience higher losses and increased torque ripple [9]. A second option is to use two isolated DC-links [10], [11], which prevents zero-sequence currents but introduces common-mode voltage issues, similar to conventional Voltage Source Inverters (VSIs). This configuration enhances system reliability by electrically isolating the two sides of the machine and eliminating circulating currents. However, it also increases the overall system cost due to the requirement of two separate power supplies and reduces control flexibility, as these sources often operate at fixed voltage levels, limiting the possibility of dynamic power sharing between the converters. The third approach is to use a Floating Capacitor as the DC-link for the Aux-Conv [12]. This eliminates zero-

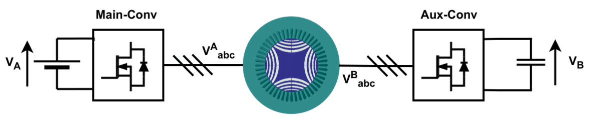

Fig. 1. SyRel in OEW with FC drive scheme.

sequence currents and allows dynamic adjustment of the FC voltage to improve the torque-speed profile [13]. By properly regulating the FC voltage, it is possible to extend the constant-torque region and delay the field-weakening transition [6]. In this work, the Floating Capacitor voltage of the Aux-Conv is also treated as a dynamic state to be actively controlled. Its charging behavior depends on the current exchanged between the Main Converter and the Auxiliary Converter through the SyRel motor.

To fully exploit the potential of multi-converter motor drives and enhance their overall performance, advanced control strategies such as Model Predictive Control (MPC) have been extensively investigated [14], [15]. MPC determines the optimal control action by solving an Integer Quadratic Optimal Control Problem (IQOCP) over a finite prediction horizon [16], [17]. Thanks to its flexible cost function, MPC can address multiple control objectives while handling system nonlinearities caused by switching operations and motor dynamics [15], [18].

However, the effectiveness of MPC in motor drive applications strongly depends on the accuracy of the system model [19]. In practical scenarios, motor parameters may vary due to changing operating conditions or environmental factors, and they are often unknown at startup [20]. This model dependency can lead to performance degradation and even control instability [21].

To overcome these limitations, MFPC has emerged as a promising alternative. Instead of relying on a detailed mathematical model, MFPC uses system input-output data to predict future behavior, reducing the need for explicit model knowledge [22]. A well-established technique in this context is the Recursive Least Squares algorithm [23]. In MFPC for electric drives, RLS is used to estimate uncertain model parameters in real time based on measured currents and voltages from previous sampling periods. This enables accurate current prediction without requiring precise motor parameters, ensuring reliable performance even under parameter mismatches [24]. The key advantage of MFPC, particularly for electric drives applications, lies in its robustness to parameter uncertainties, which translates into improved performance and stability across a wide range of operating conditions [25].

A Model-Free Predictive Control strategy is proposed, relying on two ARX models to estimate motor currents and FC voltage without requiring detailed motor information. The model parameters are identified online via RLS, and predictions are used to minimize a multivariable cost function regulating current, FC voltage, and power factor. A key contribution is the tailored formulation of the ARX model for current prediction, specifically designed for OEW SyRel drives and integrated within the FCS-MPC framework.

TABLE I
NAMEPLATE PARAMETERS OF THE SYREL MOTOR UNDER TEST.

Parameter	Symbol	Value	Unit
Stator resistance	R_s	6.3	Ω
Rated torque	T_{em}	7	Nm
Rated speed	ω_m	1500	rpm
Rated power	P_n	1.1	kW
Rated current (RMS)	I_n	4.1	A
Rated voltage (RMS)	V_n	380	V
Pole pairs	p	2	–

The paper is organized as follows: Section II describes the system and the proposed control. Section III presents simulation results. Finally, Section IV concludes the paper and outlines future work.

II. SYSTEM MODEL

A. OEW SyRel and Floating Bridge Capacitor Equations

The governing equations of a Synchronous Reluctance machine (nameplate data are reported in Tab. I) can be expressed in the rotating dq reference frame as follows [8]:

$$\boldsymbol{v}_{s_{d,q}} = R_s \boldsymbol{i}_{d,q} + \boldsymbol{L}\frac{d\boldsymbol{i}_{d,q}}{dt} - \boldsymbol{Q}\omega_r \boldsymbol{\phi}_{d,q} \tag{1}$$

$$\boldsymbol{L} = \begin{bmatrix} L_{dd}(i_d, i_q) & L_{dq}(i_d, i_q) \\ L_{qd}(i_d, i_q) & L_{qq}(i_d, i_q) \end{bmatrix} \tag{2}$$

$$\boldsymbol{Q} = \begin{bmatrix} 0 & -1 \\ 1 & 0 \end{bmatrix} \tag{3}$$

$$T_{em} = \frac{3}{2} p \left(\boldsymbol{\phi}_{d,q}^{\top} \boldsymbol{i}_{d,q} \right) \tag{4}$$

In these equations, $\boldsymbol{v}_{s_{d,q}}$ is the stator voltage vector, $\boldsymbol{i}_{d,q}$ and $\boldsymbol{\phi}_{d,q}$ are the current and flux linkage vectors in the dq reference frame, respectively. R_s denotes the stator resistance, ω_r is the rotor electrical angular speed, and p is the number of pole pairs.

The matrix $\boldsymbol{L}$ represents the differential (incremental) inductance matrix, which captures the nonlinear magnetic behavior of the machine, while $\boldsymbol{Q}$ is the orthogonal rotation matrix accounting for the cross-coupling introduced by the reference frame transformation. In practical scenarios, the off-diagonal terms L_{dq} and L_{qd} generally assume non-zero values due to magnetic saturation and saliency effects. These phenomena increase the complexity of obtaining an accurate mathematical model of the machine. In this context, a Model-Free control approach offers a significant advantage, as it eliminates the need for explicit knowledge of machine parameters and detailed magnetic characterization. Consequently, the accuracy of current predictions is no longer strictly dependent on the quality of an equivalent analytical model, improving robustness under parameter uncertainties.

The schematic of the drive system is illustrated in Fig. 1. The steady-state voltage equations are derived considering the

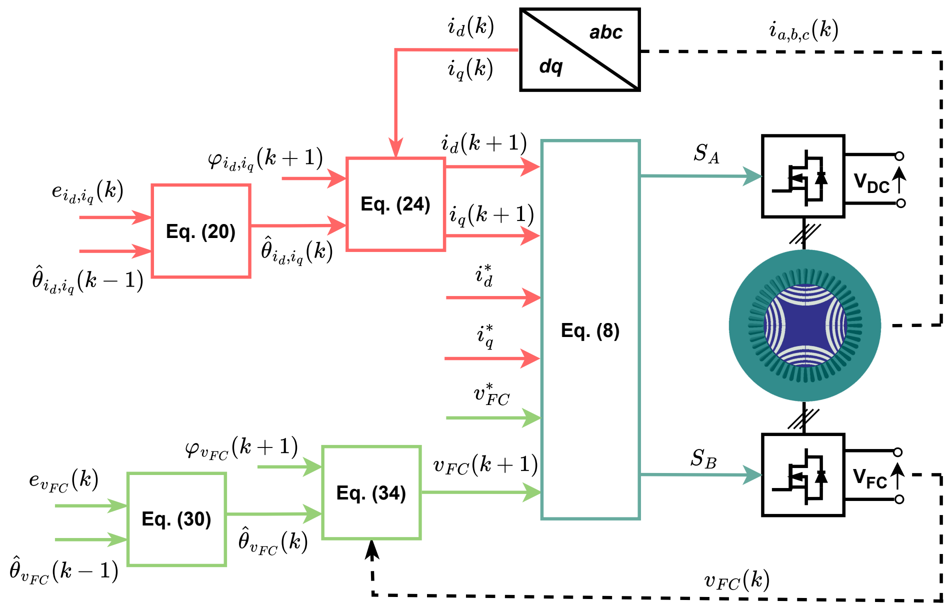

Fig. 2. Proposed control method (f= 20 kHz): (light blue) cost function; (red) dq current prediction; (green) v_{FC} prediction.

dq frame aligned with the SyRel current vector. The stator voltage of the OEW SyRel machine, in space-vector form, is given by:

$$\overline{v}_S = \overline{v}_A - \overline{v}_B \tag{5}$$

where $\overline{v}_S$ is the stator voltage space vector, and $\overline{v}_A$ and $\overline{v}_B$ are the voltage space vectors generated by the Main Converter (Main-Conv) and the Auxiliary Converter (Aux-Conv), respectively.

Transforming (5) onto the dq reference frame under steady-state conditions yields:

$$v_{Sd} = v_{Ad} - v_{Bd} \tag{6a}$$

$$v_{Sq} = v_{Aq} - v_{Bq} \tag{6b}$$

where v_{Ad} and v_{Aq} are the d- and q-axis voltage components at the output of the Main-Conv, and v_{Bd} and v_{Bq} are those corresponding to the Aux-Conv.

The Floating Capacitor, which forms the DC-link of the Aux-Conv, plays a fundamental role in the energy management of the system. Its voltage V_{FC} evolves as a function of the power exchanged between the motor and the Aux-Conv. The energy stored in the FC follows the dynamic equation:

$$\frac{d}{dt}\left(\frac{1}{2}CV_{FC}^2\right) = \frac{3}{2}\overline{i_S} \cdot \overline{v_{FC}} \tag{7}$$

where C is the capacitance of the FC, V_{FC} is its DC-link voltage, and the dot product "$\cdot$" indicates the sum of the products of the corresponding d- and q-axis components.

This formulation enables an accurate description of the energy exchange within the OEW drive system, which is essential for the effective control of both motor torque and FC voltage.

B. Control Strategy

The block diagram of the proposed MFPC algorithm, depicted in Fig. 2, predicts the system's future behavior for each actuation command. It then selects the switching state that minimizes a specified cost function, which is proportional to the difference between predictions and references. The controller has been designed to ensure the tracking of the dq current vectors and DC voltage on the FC while also compensating for the reactive power of the Main-Conv and the active power of the Aux-Conv. A single cost function incorporates three reference tracking terms. The cost function $\boldsymbol{g}(m,n)$ is expressed as (8). The first term of (8) comprises the squared two-norm of the error between the reference current $i_{d,q}^*$ and the predicted current $\mathbf{i_{d,q}}^{k+1}(m,n)$. The second term is the desired DC-link voltage on the B-side v_{FC}^*, calculated as presented in [6], and its predicted counterpart is $\mathbf{v_{FC}}^{k+1}(n)$. The indices m and n correspond to the eight configurable switching states of the Main-Conv and Aux-Conv, respectively, resulting in 64 possible combinations. T_s is the control sample time (i.e. $T_s = 5e^{-5}$s). The integral term $W_{i_{d,q}} T_s \left(\sum_{j=0}^{m} i_{d,q\ err}^{k-j}\right)$ is used to eliminate the steady-state error [14].

C. Current Prediction Method

The presented approach to predict the current and the FC voltage at $k+1$ is based on a RLS algorithm to identify the parameters of an ARX model [26], [27].

The SyRel and the Floating Capacitor are considered as a black-box. This means that both the structure and the parameters of the model must first be estimated before making predictions. ARX popularity stems from the fact that its parameters can be efficiently estimated using well-known methods

$$\mathbf{g}\left(m,n\right)=\left\|i^{*}_{d,q}-\boldsymbol{i_{d,q}}^{\;k+1}(m,n)+W_{i_{d,q}}T_{s}\left(\sum_{z=0}^{l}\boldsymbol{i_{d,q\;err}}^{k-z}\right)\right\|_{2}^{2}+w_{v_{FC}}\left\|v^{*}_{FC}-\boldsymbol{v_{FC}}^{k+1}(n)\right\|_{2}^{2} \tag{8}$$

$$\mathbf{\hat{i}}(k)=\frac{1}{\mathbf{A}(z^{-1})}[\mathbf{B_{A}}(z^{-1})\mathbf{v_{A}}(k)+\mathbf{B_{B}}(z^{-1})\mathbf{v_{B}}(k)+\mathbf{C}(z^{-1})\mathbf{i}(k)] \tag{9}$$

like RLS. In addition, ARX models remain effective even when nonlinearities are present, improving the robustness of the prediction process [28]. For these reasons, this work uses an ARX model as the foundation of the black-box prediction in the proposed predictive control strategy. The ARX-based representation defines a transfer function between the input voltage and the output stator currents in the dq stationary reference defined as (9). In (9), z^{-1} denotes the unit delay operator and is used to express the dependence of the current output on past values of voltages and currents in the discrete-time domain. The estimated currents ($\hat{i_d}(k)$ and $\hat{i_q}(k)$), the measured currents ($i_d(k)$ and $i_q(k)$), and control voltages ($v_{Ad}(k)$, $v_{Aq}(k)$, $v_{Bd}(k)$ and $v_{Bq}(k)$) are defined as follows:

$$\mathbf{\hat{i}}(k)=\begin{bmatrix}\hat{i_d}(k)\\ \hat{i_q}(k)\end{bmatrix} \tag{10}$$

$$\mathbf{i}(k)=\begin{bmatrix}i_d(k)\\ i_q(k)\end{bmatrix} \tag{11}$$

$$\mathbf{v_A}(k)=\begin{bmatrix}v_{Ad}(k)\\ v_{Aq}(k)\end{bmatrix} \tag{12}$$

$$\mathbf{v_B}(k)=\begin{bmatrix}v_{Bd}(k)\\ v_{Bq}(k)\end{bmatrix} \tag{13}$$

The coefficients used in the ARX models are given in equations (14), (15), (16), and (17). The ARX model structure is determined by the polynomial orders n_A, n_B, and n_C, which in this work are chosen as $n_A = 3$, $n_B = 2$, and $n_C = 2$ [26].

Specifically, the matrix $\mathbf{A}(z^{-1})$ contains the auto regressive polynomials $\mathbf{A}^d(z^{-1})$ and $\mathbf{A}^q(z^{-1})$ along the diagonal, capturing the dependence of the d- and q-axis current components on their past values. The matrices $\mathbf{B_A}(z^{-1})$ and $\mathbf{B_B}(z^{-1})$ define the system response to the voltages applied by Main-Conv and Aux-Conv, respectively. Each consists of diagonal elements $\mathbf{B^{Ad}}(z^{-1})$, $\mathbf{B^{Aq}}(z^{-1})$, $\mathbf{B^{Bd}}(z^{-1})$, and $\mathbf{B^{Bq}}(z^{-1})$, representing the contribution of input voltages in each axis. The matrix $\mathbf{C}(z^{-1})$ accounts for the cross-coupling between the d and q axes through the off-diagonal terms $\mathbf{C^{dq}}(z^{-1})$ and $\mathbf{C^{qd}}(z^{-1})$. All polynomials are expressed in terms of the backward shift operator z^{-1}, with the associated coefficients a_i, b_i, and c_i determining the model dynamics.

By performing the calculations and substituting the coefficients into (9), the estimates of the d-axis and q-axis currents are obtained. These estimates, shown in (18) and (19), are then used for prediction.

The RLS algorithm is applied to estimate the coefficients (14), (15), (16), and (17) of the ARX model, using measurements collected from the controlled system. The RLS algorithm is based on a set of recursive equations, where the goal at each iteration is to accurately estimate the parameter vectors $\boldsymbol{\hat{\theta}_{i_d,i_q}}(k)$:

$$\boldsymbol{\hat{\theta}_{i_d,i_q}}\left(k\right)=\boldsymbol{\hat{\theta}_{i_d,i_q}}\left(k-1\right)+\mathbf{G}_{i_d,i_q}\left(k\right)e_{i_d,i_q}\left(k\right) \tag{20}$$

given that

$$\boldsymbol{G_{i_d,i_q}}(k)=\frac{\boldsymbol{P_{i_d,i_q}}(k-1)\boldsymbol{\varphi_{i_d,i_q}}(k)}{\boldsymbol{\varphi^{T}_{i_d,i_q}}(k)\boldsymbol{P_{i_d,i_q}}(k-1)\boldsymbol{\varphi_{i_d,i_q}}(k)+\lambda}, \tag{21}$$

and

$$\boldsymbol{P_{i_d,i_q}}(k)=\frac{1}{\lambda}(\boldsymbol{I}-\boldsymbol{G_{i_d,i_q}}(k)\boldsymbol{\varphi^{T}_{i_d,i_q}}(k))\boldsymbol{P_{i_d,i_q}}(k-1). \tag{22}$$

The matrix $\boldsymbol{P}_{i_d,i_q}(k)$ represents the covariance matrix used in the RLS algorithm. The gain matrices $\mathbf{G_{i_d,i_q}}(k)$ link the updated parameters vector at each sampling step with the estimation errors $e_{i_d,i_q}\left(k\right)$ given by:

$$e_{i_d,i_q}\left(k\right)=M_{i_d,i_q}(k)-\boldsymbol{\varphi_{i_d,i_q}}^{T}\left(k\right)\boldsymbol{\hat{\theta}_{i_d,i_q}}\left(k-1\right) \tag{23}$$

where $M_{i_d,i_q}(k)$ are the instantaneous measurements of d and q current components, respectively. The forgetting factor $0 < \lambda \leq 1$ is used in the RLS algorithm to give more importance to recent measurements [26]. Lower values of λ allow the algorithm to quickly follow changes in system parameters, but also increase its sensitivity to noise [29]. In this work, λ is set to 1 to improve noise rejection, as the controller operates at a high sampling rate and parameter variations are expected to be slow.

The prediction for each possible switching state (m,n) is computed as the scalar product:

$$\mathbf{i_{d,q}}^{k+1}(m,n)=\boldsymbol{\varphi_{i_d,i_q}}^{k+1}\left(m,n\right)\cdot\boldsymbol{\hat{\theta}_{i_d,i_q}}\left(k\right) \tag{24}$$

where $\varphi_{\mathbf{i_d},\mathbf{i_q}}{}^{k+1}\left(m,n\right)$ are defined as:

$$\boldsymbol{\varphi_{i_d}}^{k+1}(m,n)=\begin{bmatrix}i_d(k)\\ i_d(k-1)\\ i_d(k-2)\\ i_q(k)\\ i_q(k-1)\\ v_{Ad}(m)\\ v_{Ad}(k)\\ v_{Bd}(n)\\ v_{Bd}(k)\end{bmatrix} \tag{25}$$

$$\mathbf{A}(z^{-1}) = \begin{bmatrix} \mathbf{A^d}(z^{-1}) & 0 \\ 0 & \mathbf{A^q}(z^{-1}) \end{bmatrix} = \begin{bmatrix} 1-\sum_{i=1}^{n_A} a_i^d z^{-1} & 0 \\ 0 & 1-\sum_{i=1}^{n_A} a_i^q z^{-1} \end{bmatrix} \tag{14}$$

$$\mathbf{B_A}(z^{-1}) = \begin{bmatrix} \mathbf{B^{Ad}}(z^{-1}) & 0 \\ 0 & \mathbf{B^{Aq}}(z^{-1}) \end{bmatrix} = \begin{bmatrix} \sum_{i=0}^{n_B} b_i^{Ad} z^{-1} & 0 \\ 0 & \sum_{i=0}^{n_B} b_i^{Aq} z^{-1} \end{bmatrix} \tag{15}$$

$$\mathbf{B_B}(z^{-1}) = \begin{bmatrix} \mathbf{B^{Bd}}(z^{-1}) & 0 \\ 0 & \mathbf{B^{Bq}}(z^{-1}) \end{bmatrix} = \begin{bmatrix} \sum_{i=0}^{n_B} b_i^{Bd} z^{-1} & 0 \\ 0 & \sum_{i=0}^{n_B} b_i^{Bq} z^{-1} \end{bmatrix} \tag{16}$$

$$\mathbf{C}(z^{-1}) = \begin{bmatrix} 0 & \mathbf{C^{dq}}(z^{-1}) \\ \mathbf{C^{qd}}(z^{-1}) & 0 \end{bmatrix} = \begin{bmatrix} 0 & \sum_{i=0}^{n_C} c_i^{dq} z^{-1} \\ \sum_{i=0}^{n_C} c_i^{qd} z^{-1} & 0 \end{bmatrix} \tag{17}$$

$$\hat{i_d}(k) = \frac{\mathbf{B^{Ad}}(z^{-1})}{\mathbf{A^d}(z^{-1})} v_{Ad}(k) + \frac{\mathbf{B^{Bd}}(z^{-1})}{\mathbf{A^d}(z^{-1})} v_{Bd}(k) + \frac{\mathbf{C^{dq}}(z^{-1})}{\mathbf{A^d}(z^{-1})} i_q(k) \tag{18}$$

$$\hat{i_q}(k) = \frac{\mathbf{B^{Aq}}(z^{-1})}{\mathbf{A^q}(z^{-1})} v_{Aq}(k) + \frac{\mathbf{B^{Bq}}(z^{-1})}{\mathbf{A^q}(z^{-1})} v_{Bq}(k) + \frac{\mathbf{C^{qd}}(z^{-1})}{\mathbf{A^q}(z^{-1})} i_d(k) \tag{19}$$

$$\boldsymbol{\varphi}_{\boldsymbol{i_q}}{}^{k+1}(m,n) = \begin{bmatrix} i_q(k) \\ i_q(k-1) \\ i_q(k-2) \\ i_d(k) \\ i_d(k-1) \\ v_{Aq}(m) \\ v_{Aq}(k) \\ v_{Bq}(n) \\ v_{Bq}(k) \end{bmatrix} \tag{26}$$

D. FC Prediction Method

The FC voltage is also predicted using an ARX model, which relates the DC current $i_{DC}(k)$ to the FC voltage $v_{FC}(k)$. The $i_{DC}(k)$ is estimated by the control algorithm based on the stator current components. The adopted ARX model is expressed as:

$$\hat{v}_{FC}(k) = \frac{\mathbf{D}(z^{-1})}{\mathbf{E}(z^{-1})} i_{DC}(k) \tag{27}$$

The polynomial coefficients, $\mathbf{D}(z^{-1})$ and $\mathbf{E}(z^{-1})$, used in the ARX model for the Floating Capacitor voltage in (27) are defined as follows:

$$\mathbf{E}(z^{-1}) = 1 - \sum_{i=1}^{n_E} e_i z^{-1} \tag{28}$$

$$\mathbf{D}(z^{-1}) = \sum_{i=0}^{n_D} d_i z^{-1} \tag{29}$$

For the FC voltage, the ARX model structure is defined by the polynomial orders n_D and n_E, which are set to $n_D = 3$ and $n_E = 2$.

The RLS algorithm is applied to estimate the coefficients (28), and (29) of the ARX model, using measurements collected from the controlled system. The RLS algorithm is based on a set of recursive equations, where the goal at each iteration is to accurately estimate the parameter vectors $\hat{\mathbf{v}}_{\mathbf{FC}}(k)$:

$$\hat{\boldsymbol{\theta}}_{\boldsymbol{v_{FC}}}(k) = \hat{\boldsymbol{\theta}}_{\boldsymbol{v_{FC}}}(k-1) + \mathbf{G}_{v_{FC}}(k)\, e_{v_{FC}}(k) \tag{30}$$

where

$$\boldsymbol{G}_{\boldsymbol{v_{FC}}}(k) = \frac{\boldsymbol{P}_{\boldsymbol{v_{FC}}}(k-1)\boldsymbol{\varphi}_{\boldsymbol{v_{FC}}}(k)}{\boldsymbol{\varphi}^{\boldsymbol{T}}_{\boldsymbol{v_{FC}}}(k)\boldsymbol{P}_{\boldsymbol{v_{FC}}}(k-1)\boldsymbol{\varphi}_{\boldsymbol{v_{FC}}}(k) + \lambda}, \tag{31}$$

and

$$\boldsymbol{P}_{\boldsymbol{v_{FC}}}(k) = \frac{1}{\lambda}(\boldsymbol{I} - \boldsymbol{G}_{\boldsymbol{v_{FC}}}(k)\boldsymbol{\varphi}^{\boldsymbol{T}}_{\boldsymbol{v_{FC}}}(k))\boldsymbol{P}_{\boldsymbol{v_{FC}}}(k-1). \tag{32}$$

The gain matrices $\mathbf{G}_{\mathbf{v_{FC}}}(k)$ link the updated parameters vector at each sampling step with the estimation errors $e_{v_{FC}}(k)$ given by:

$$e_{v_{FC}}(k) = M_{v_{FC}}(k) - \boldsymbol{\varphi}_{\boldsymbol{v_{FC}}}{}^{T}(k)\, \hat{\boldsymbol{\theta}}_{\boldsymbol{v_{FC}}}(k-1) \tag{33}$$

where $M_{v_{FC}}(k)$ is the measured FC voltage at time k. The forgetting factor λ is also set to 1. The predictions are computed as the scalar product:

$$\mathbf{v_{FC}}^{k+1}(n) = \boldsymbol{\varphi}_{\boldsymbol{v_{FC}}}{}^{k+1}(n) \cdot \hat{\boldsymbol{\theta}}_{\boldsymbol{v_{FC}}}(k) \tag{34}$$

where $\boldsymbol{\varphi}_{\boldsymbol{v_{FC}}}{}^{k+1}(n)$ is defined as:

$$\boldsymbol{\varphi}_{\boldsymbol{v_{FC}}}(k+1) = \begin{bmatrix} v_{FC}(n) \\ v_{FC}(k) \\ v_{FC}(k-1) \\ i_{DC}(k) \\ i_{DC}(k-1) \end{bmatrix} \tag{35}$$

The pair (m, n) that minimizes (8) is selected to apply to the system at the desired operating point in the next time step.

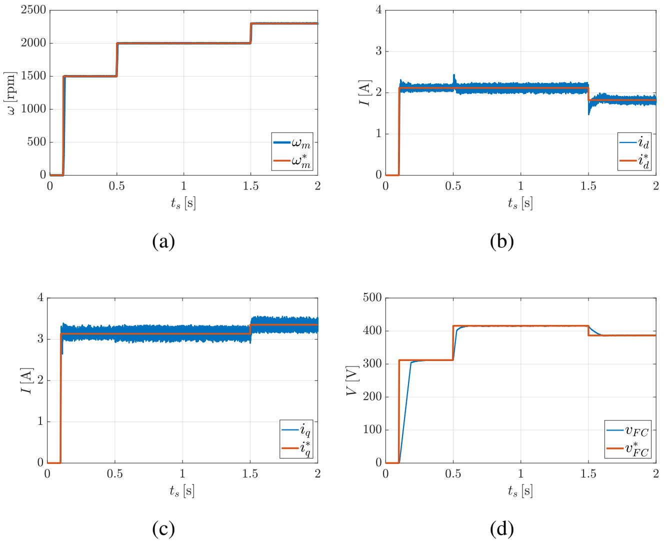

Fig. 3. Simulation results for different operating points: (a) ω_m tracking; (b) i_d tracking; (c) i_q tracking; (d) v_{FC} tracking.

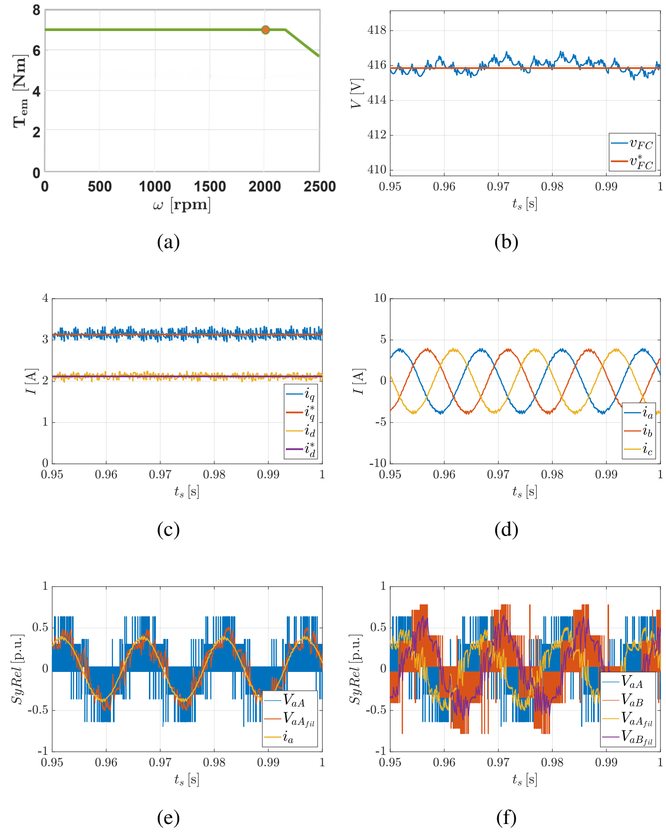

Fig. 4. Simulation results at steady-state (2000 rpm): (a) Torque-Speed characteristic; (b) v_{FC}; (c) i_d and i_q; (d) i_{abc}; (e) Main-Conv a-phase voltage and current; (f) Main-Conv and Aux-Conv a-phase voltages.

III. Simulation Results

This section presents simulation results that validate the effectiveness of the proposed control strategy applied to an OEW-SyRel motor drive. The Main-Conv is supplied by a constant voltage source set to 600 V. This value is approximately 10% higher than the typical rated voltage and was intentionally selected to operate at a lower modulation index, providing a higher voltage margin during high-speed operation to ensure the desired speed and torque targets are reliably achieved during the tests. The FC voltage of the Aux-Conv is directly regulated by the control algorithm. The control sampling rate is set to 5×10^{-5} s. The initial values of the ARX model parameters θ have been identified through a trial-and-error procedure to guarantee satisfactory model accuracy also at the system's initial operating point. The simulations have been performed in MATLAB, Simulink.

The control structure simultaneously regulates the dq current components and the FC voltage of the Aux-Conv. The rotational speed is managed by a prime mover and its profile is shown in Fig. 3(a). During the first time interval ($0.5 < t < 1.5$ s), the speed is set to 2000 rpm, exceeding the base speed of the standard SyRel configuration (1500 rpm) due to the additional reactive power supplied by the FC. In the second time interval ($1.5 < t < 2.5$ s), the speed is increased to 2300 rpm, thus entering the flux-weakening region.

Fig. 3(b), 3(c) and 3(d) show the tracking performance of the dq current components and the FC voltage for three different operating points: 1500 rpm and 2000 rpm under rated torque ($i_d = 2.118$ A, $i_q = 3.134$ A), and a first flux-weakening point at 2300 rpm ($i_d = 1.824$ A, $i_q = 3.352$ A). Fig. 3(b) shows the i_d current tracking. A slight transient spike is observed at $t = 0.5$ s, corresponding to the speed increase from 1500 to 2000 rpm. A similar spike occurs at $t = 1.5$ s, during the second speed transition into the flux-weakening region. These transients are acceptable considering the system dynamics. Fig. 3(c) shows the i_q current tracking, which exhibits a short settling time. Its smooth behavior ensures constant torque delivery during speed variations. Fig. 3(d) presents the FC voltage tracking, where the feedback perfectly follows the reference, which is computed based on the initial dataset and following the approach proposed in [6].

Fig. 4 and 5 provide a steady-state analysis of the system for 2000 and 2300 rpm, respectively. The torque-speed limit curve, illustrated in Fig. 4(a), is obtained from the analysis in [6], which considers the FC's capability to extend the base speed beyond the standard SyRel operation. Fig. 4(b) shows the FC voltage at steady state. Fig. 4(c) and 4(d) report the dq and three-phase currents, respectively, with a Total Harmonic Distortion (THD) of 3.78%, 3.65%, and 3.82% for i_a, i_b, and i_c, respectively.

Fig. 4(e) illustrates that at 2000 rpm there is no phase shift between the phase current i_a and the corresponding output voltage v_{aA} of the Main-Conv. Conversely, Fig. 4(f) shows a 90° phase shift between the a-phase voltage and the corresponding output voltage v_{aB} of the Aux-Conv. This behavior confirms that the reactive power provided by the Aux-Conv fully compensates the reactive demand, and no active power is exchanged between the motor and the Aux-Conv. The FC actively supplies the system with reactive power, ensuring

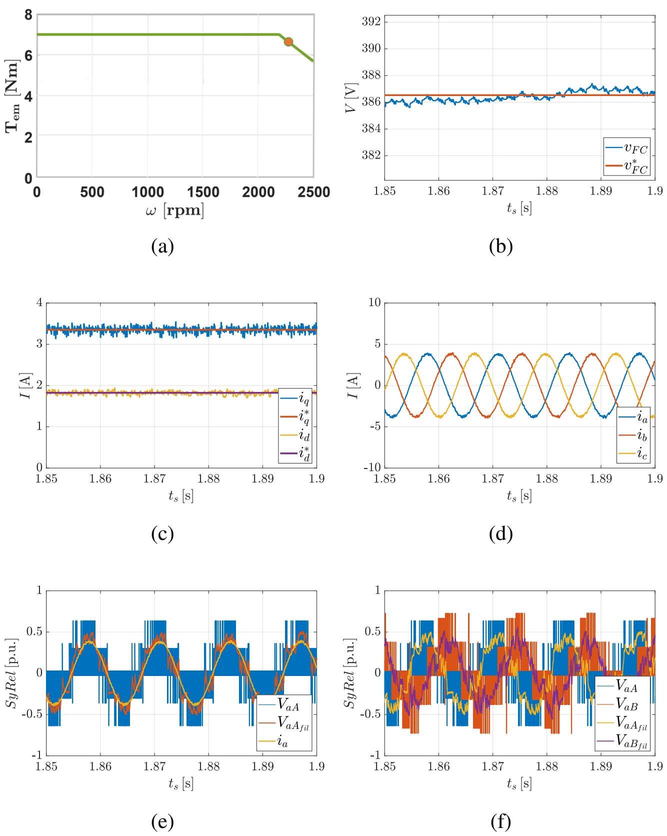

Fig. 5. Simulation results at steady-state ($2300\,\mathrm{rpm}$): (a) Torque-Speed characteristic; (b) v_{FC}; (c) i_d and i_q; (d) i_{abc}; (e) Main-Conv a-phase voltage and current; (f) Main-Conv and Aux-Conv a-phase voltages.

unity power factor on the Main-Conv side and enhancing the overall efficiency.

Similar behavior is observed for the flux-weakening region at $2300\,\mathrm{rpm}$, as shown in Fig. 5. Compared to the $2000\,\mathrm{rpm}$ case, the FC continues to provide effective reactive power compensation, maintaining unitary power factor on the Main-Conv and stable system operation even at higher speeds.

Finally, Fig. 6 shows the system's dynamic response to a torque step. As illustrated in Fig. 6(a), the speed is set to $500\,\mathrm{rpm}$ with zero torque, followed by an application of rated torque. A comparison is made with the Model-Based control strategy proposed in [4] to demonstrate the feasibility of the proposed Model-Free approach. Fig. 6(b), Fig. 6(c) and Fig. 6(d) show that both current and voltage control exhibit similar dynamic behavior, despite the absence of an accurate system model.

These results highlight a key advantage of the MF approach: it avoids precise system identification, simplifying commissioning and improving robustness to parameter uncertainties. Although FC voltage control is inherently slower than current control, the predictive strategy effectively handles both fast and slow dynamics within a unified cost function. However, some practical limitations must be considered. Model parameter estimation typically requires a transient phase, which can degrade performance at startup. Additionally, the higher computational

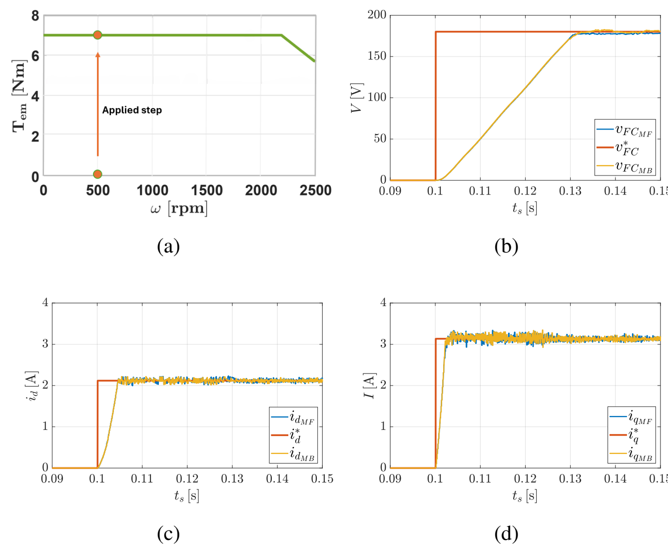

Fig. 6. Simulation results at step variation at $500\,\mathrm{rpm}$ (Model-Based vs Model-Free): (a) Torque-Speed characteristic; (b) v_{FC}; (c) i_d; (d) i_q.

complexity compared to conventional schemes may restrict its use on platforms with limited processing resources.

IV. Conclusions

This paper has presented a MFPC strategy for OEW-SyRel motor drives supplied by a Main Converter and an Auxiliary Converter equipped with a Floating Capacitor. The proposed control scheme simultaneously regulates the torque and the floating capacitor voltage level, effectively extending the operational speed range beyond the base speed compared to conventional Single Inverter operation, while ensuring unity power factor on the Main Converter side. A unified cost function governs both currents and floating capacitor voltage control, allowing for coordinated management of fast and slow dynamics without requiring an explicit motor model.

Simulation results demonstrate the capability of the proposed approach to achieve accurate torque tracking, voltage regulation, and seamless operation in both constant torque and flux-weakening regions. Furthermore, the MFPC approach eliminates the need for precise motor parameter identification and complex system modeling, simplifying the control design and enhancing robustness against parameter uncertainties.

The effectiveness of the proposed control strategy is further confirmed through comparative analysis with state-of-the-art model-based solutions, highlighting its suitability for high-performance OEW-SyRel drives with minimal system knowledge requirements.

Acknowledgment

This work was supported by the Marie Skłodowska-Curie Actions (MSCA) under the European Union's Horizon 2020 Research and Innovation Staff Exchange (RISE) under Grant 872001.

REFERENCES

[1] M. Murataliyev, M. Degano, M. Di Nardo, N. Bianchi, and C. Gerada, "Synchronous reluctance machines: A comprehensive review and technology comparison," *Proceedings of the IEEE*, vol. 110, no. 3, pp. 382–399, 2022.

[2] N. Bianchi, S. Bolognani, E. Carraro, M. Castiello, and E. Fornasiero, "Electric vehicle traction based on synchronous reluctance motors," *IEEE Transactions on Industry Applications*, vol. 52, no. 6, pp. 4762–4769, 2016.

[3] G. De Boni, L. Mantione, M. Minervini, and L. Frosini, "Look-up table based reduced order model of synchronous motors for digital twin applications," in *2025 IEEE Workshop on Electrical Machines Design, Control and Diagnosis (WEMDCD)*, 2025, pp. 1–6.

[4] F. Gemma, J. Riccio, G. Tresca, O. Benfatto, and P. Zanchetta, "Finite-control-set model-predictive control of open-end winding synchronous reluctance motor drives," in *2025 IEEE Workshop on Electrical Machines Design, Control and Diagnosis (WEMDCD)*, 2025, pp. 1–6.

[5] A. Amerise, L. Rovere, A. Formentini, M. Mengoni, L. Zarri, and P. Zanchetta, "Electric drive based on an open-end winding surface PM synchronous machine with a floating capacitor bridge," *IEEE Transactions on Industry Applications*, vol. 56, no. 3, pp. 2709–2718, 2020.

[6] J. Riccio, F. Gemma, L. Rovere, G. Tresca, M. D. Nardo, S. Odhano, M. Degano, and P. Zanchetta, "Effects of the floating capacitor voltage on the torque-speed characteristic of an open-end winding synchronous reluctance motor drive," *IEEE Transactions on Industry Applications*, vol. 61, no. 2, pp. 3269–3278, 2025.

[7] L. Rovere, A. Formentini, G. L. Calzo, P. Zanchetta, and T. Cox, "IGBT-SiC dual fed open end winding PMSM drive," in *2017 IEEE International Electric Machines and Drives Conference (IEMDC)*, 2017, pp. 1–7.

[8] M. Zerdani, S. A. E. M. Ardjoun, H. Chafouk, and M. Denaï, "Experimental investigation of decoupled discontinuous pwm strategies in open-end winding induction motor supplied by a common dc-link," *IEEE Journal of Emerging and Selected Topics in Power Electronics*, vol. 11, no. 3, pp. 3087–3096, 2023.

[9] X. Yuan, C. Zhang, and S. Zhang, "Torque ripple suppression for open-end winding permanent-magnet synchronous machine drives with predictive current control," vol. 67, no. 3, 2020, pp. 1771–1781.

[10] J. Kalaiselvi and S. Srinivas, "Bearing currents and shaft voltage reduction in dual-inverter-fed open-end winding induction motor with reduced CMV PWM methods," *IEEE Transactions on Industrial Electronics*, vol. 62, no. 1, pp. 144–152, 2015.

[11] E. L. Soares, C. B. Jacobina, N. B. de Freitas, N. Rocha, A. C. N. Maia, and A. M. N. Lima, "A multilevel open-end winding six-phase induction motor drive topology based on three two-level three-phase inverters," *IEEE Transactions on Industry Applications*, vol. 59, no. 5, pp. 6360–6372, 2023.

[12] S. Chowdhury, P. W. Wheeler, C. Patel, and C. Gerada, "A multilevel converter with a floating bridge for open-end winding motor drive applications," vol. 63, no. 9, 2016, pp. 5366–5375.

[13] L. Rovere, G. Valente, A. Formentini, and P. Zanchetta, "Parameters and volt–ampere ratings of a floating capacitor open-end winding synchronous motor drive for extended CPSR," *IEEE Transactions on Industrial Electronics*, vol. 69, no. 5, pp. 4576–4586, 2022.

[14] F. Gemma, J. Riccio, G. Tresca, A. Volpini, and P. Zanchetta, "Finite-control-set model predictive control with reduced computational burden in cascaded h-bridge permanent magnet synchronous motor drives for ev applications," in *2024 IEEE Energy Conversion Congress and Exposition (ECCE)*, 2024, pp. 3941–3947.

[15] J. Riccio, L. Rovere, S. Odhano, M. Di Nardo, and P. Zanchetta, "Model-predictive control of open-end winding synchronous reluctance motor drives," in *2022 IEEE Energy Conversion Congress and Exposition (ECCE)*, 2022, pp. 1–8.

[16] P. Karamanakos and T. Geyer, "Guidelines for the design of finite control set model predictive controllers," *IEEE Transactions on Power Electronics*, vol. 35, no. 7, pp. 7434–7450, 2020.

[17] A. Volpini, S. R. D. Salvo, G. Tresca, R. Leuzzi, and P. Zanchetta, "A unified modulated model predictive control for a two-stage ac-dc converter interfacing a vanadium redox flow battery," *IEEE Transactions on Industry Applications*, pp. 1–11, 2025.

[18] F. Gemma, G. Tresca, A. Formentini, and P. Zanchetta, "Balanced charging algorithm for chb in an ev powertrain," *Energies*, vol. 16, no. 14, 2023. [Online]. Available: https://www.mdpi.com/1996-1073/16/14/5565

[19] M. Khalilzadeh, S. Vaez-Zadeh, J. Rodriguez, and R. Heydari, "Model-free predictive control of motor drives and power converters: A review," *IEEE Access*, vol. 9, pp. 105 733–105 747, 2021.

[20] G. Dong, Z. Zhu, Y. Lou, J. Yu, L. Wu, and J. Wei, "Optimal charging of lithium-ion battery using distributionally robust model predictive control with wasserstein metric," *IEEE Transactions on Industrial Informatics*, vol. 20, no. 5, pp. 7630–7640, 2024.

[21] P. Li, J. Hao, H. Tang, X. Fu, Y. Zhen, and K. Tang, "Bridging evolutionary algorithms and reinforcement learning: A comprehensive survey on hybrid algorithms," *IEEE Transactions on Evolutionary Computation*, pp. 1–1, 2024.

[22] A. Alessio and A. Bemporad, *A Survey on Explicit Model Predictive Control*. Berlin, Heidelberg: Springer Berlin Heidelberg, 2009, pp. 345–369. [Online]. Available: https://doi.org/10.1007/978-3-642-01094-1_29

[23] J. Hu and K. W. E. Cheng, "Predictive control of power electronics converters in renewable energy systems," *Energies*, vol. 10, no. 4, 2017. [Online]. Available: https://www.mdpi.com/1996-1073/10/4/515

[24] P. Cortes, M. P. Kazmierkowski, R. M. Kennel, D. E. Quevedo, and J. Rodriguez, "Predictive control in power electronics and drives," *IEEE Transactions on Industrial Electronics*, vol. 55, no. 12, pp. 4312–4324, 2008.

[25] S. Vazquez, J. Rodriguez, M. Rivera, L. G. Franquelo, and M. Norambuena, "Model predictive control for power converters and drives: Advances and trends," *IEEE Transactions on Industrial Electronics*, vol. 64, no. 2, pp. 935–947, 2017.

[26] J. Rodríguez, R. Heydari, Z. Rafiee, H. A. Young, F. Flores-Bahamonde, and M. Shahparasti, "Model-free predictive current control of a voltage source inverter," *IEEE Access*, vol. 8, pp. 211 104–211 114, 2020.

[27] C. González-Castaño, F. Flores-Bahamonde, H. Young, R. Heydari, S. Sabzevari, and J. Rodriguez, "Model-free predictive control based on arx representation: A comparative assessment with proportional-integral regulator," in *2021 IEEE International Conference on Predictive Control of Electrical Drives and Power Electronics (PRECEDE)*, 2021, pp. 953–958.

[28] F. Tinazzi, P. G. Carlet, S. Bolognani, and M. Zigliotto, "Motor parameter-free predictive current control of synchronous motors by recursive least-square self-commissioning model," *IEEE Transactions on Industrial Electronics*, vol. 67, no. 11, pp. 9093–9100, 2020.

[29] D. Park, B. Jun, and J. Kim, "Fast tracking rls algorithm using novel variable forgetting factor with unity zone," *Electronics Letters*, vol. 27, pp. 2150–2151, 1991. [Online]. Available: https://digital-library.theiet.org/doi/abs/10.1049/el%3A19911331